Engineering Fracture Mechanics 268 (2022) 108460

Contents lists available at ScienceDirect

Engineering Fracture Mechanics

journal homepage: www.elsevier.com/locate/engfracmech

# Fatigue limit evaluation via infrared thermography for a high strength steel with two strength levels

Aiguo Zhao [a], Jijia Xie [b,c], Yingxin Zhao [d], Chuang Liu [a], Junchen Zhu [a], Guian Qian [b,c], Shuguang Wang [a,*], Youshi Hong [b,c,*]

[a] College of Civil Engineering, Nanjing Tech University, Nanjing 211816, China
[b] State Key Laboratory of Nonlinear Mechanics, Institute of Mechanics, Chinese Academy of Sciences, Beijing 100190, China
[c] School of Engineering Science, University of Chinese Academy of Sciences, Beijing 100049, China
[d] Standards & Metrology Research Institute, China Academy of Railway Sciences Corporation Limited, Beijing 10081, China

ARTICLE INFO

*Keywords:*
High-cycle fatigue
Intrinsic dissipation
Damage accumulation mechanism
Microplasticity
Infrared thermography

ABSTRACT

The fatigue limit of a high strength steel (GCr15) with two strength levels (2372 MPa and 1044 MPa) was evaluated in terms of energy dissipation during high-cycle fatigue (HCF) and very-high-cycle fatigue (VHCF) process. Two methods based on the maximum temperature variation and intrinsic energy dissipation were used to assess the fatigue limit and the predicted results were in agreement with those of conventional fatigue tests. The grain boundary of tempered martensite for the specimen group with higher strength acts as barriers to resist dislocation gliding and multiplication, and thus it behaves lower heat dissipation and higher fatigue strength than the specimen group with lower strength.

## 1. Introduction

The fatigue property of mechanical components is the most important factor in structural design. However, the assessment of fatigue property is a time-consuming and labor-intensive process [1]. Especially in high-cycle fatigue (HCF) and very-high-cycle fatigue (VHCF) regimes, the traditional experimental methods usually take a very long period and high cost to obtain the S-N curve and fatigue limit for just one specific material and one loading type [2]. Several theories and methods have been proposed to assess the fatigue properties of materials rapidly, which are based on the temperature elevation of specimens during fatigue loading [3–7]. The temperature elevation phenomenon is also named as self-heating effect, which is caused by the energy dissipation resulted from cyclic loading [8–11].

Irreversible microstructure degradation such as dislocation multiplication and microplasticity will lead to damage accumulation and failure. The material behaves elastically macroscopically in HCF and VHCF regimes, and thus it is almost impossible to assess the process through conventional detection means. On the contrary, the fatigue energy dissipation provides a beneficial detection means to assess the fatigue damage evolution macroscopically. The temperature variation is usually detected by infrared thermographic technique. As observed in most experiments, the temperature of specimens increases firstly, then approaches to a stabilization stage, and finally increases abruptly until failure. Different applied stress amplitudes will lead to different stabilized temperature variations. In the beginning, temperature variation of specimen under different stress amplitudes during fatigue loading was utilized to predict

* Corresponding authors.
*E-mail addresses:* 720108@vip.sina.com (S. Wang), hongys@imech.ac.cn (Y. Hong).

https://doi.org/10.1016/j.engfracmech.2022.108460
Received 13 February 2022; Received in revised form 2 April 2022; Accepted 8 April 2022
Available online 12 April 2022

fatigue limits and S-N curves [12–25]. It is observed that the temperature variation increases abruptly at a constant stress amplitude, which is taken as the fatigue limit. Although this empirical method is proved to be very successful for many materials with low strength and apparent temperature rise, there is no distinct physical basis. Besides, the temperature variation could be influenced by many factors such as surrounding temperature and air condition. The temperature variation is not the most relevant physical parameter to assess damage evolution. Thus, a direct and much more relevant damage indicator is required in this regard. The fatigue intrinsic dissipation derived from temperature variation has been commonly accepted as a more appropriate damage indicator [26–29]. This indicator motivates researchers to establish different thermal conduction equations based on measured temperature signals to get a more accurate calculation of fatigue intrinsic dissipation.

The accurate calculation of intrinsic dissipation relies on the effective deduction of heat diffusion equation and the precise capture of temperature distribution field map of specimens. Several models have been proposed in the past decades for estimating fatigue intrinsic dissipation on different materials [30–43]. The differences among such models are the methods of simplifying heat diffusion equation and those of deducing intrinsic dissipation from experimental temperature distribution data. However, the energy dissipation process is sensitive to the microstructure status and surrounding environments. Due to the different simplifying conditions of proposed models and the parameter scatter of fitting line from experimental data, a certain deviation always exists for these predictions, which may result in different fatigue properties. The theoretical models established for calculating intrinsic dissipation are still not well recognized. Besides, the infrared thermography method was proven to be applicable to materials with low strength such as low-strength steels, where the reported investigations have shown that there is an obvious sign of fatigue limit [3–7]. But for materials with high strength, it is shown that fatigue failures still occur in the VHCF regime beyond $10^7$ loading cycles and there is still no clear presence of fatigue limit. In fact, it is the fatigue strength at $10^7$ loading cycles. However, the phrase “fatigue limit at $10^7$ loading cycles” is still adopted for these materials by many researchers. So far, whether the infrared thermography method is applicable to high strength materials is still unknown.

In this paper, the fatigue intrinsic dissipation during HCF and VHCF processes is utilized to assess the fatigue limit of a bearing steel (GCr15) with two different strength levels. The fatigue limits obtained by infrared thermography based on the maximum temperature variation and intrinsic energy dissipation are compared with those obtained by conventional fatigue tests. Then an FEM simulation is performed to verify the assumptions and the experimental results. For the purpose of explaining the damage accumulation evolution during fatigue loading qualitatively, the F-R (Frank-Read) dislocation multiplication model is used to address the fatigue strength difference between the two specimen groups. A two probabilistic multiscale model is adopted to further assess the fatigue limit and characterize the microplasticity activation resistance of a material quantitatively.

## 2. Theoretical background of self-heating in fatigue loading

Thin-plate specimen whose thickness is much smaller than its length and width was generally adopted in the fatigue experiment of infrared thermography. A dimensionless parameter named as Biot number has been utilized to assess the ratio of heat transfer resistance between the interior and the surface of an object [44,45]:

$$Bi = \frac{h_c L}{k} \tag{1}$$

where $k$ is the material thermal conductivity, $h_c$ is the heat convection coefficient with the surroundings, and $L$ is the length of specimen.

Suppose the convection coefficient $h_c = 5 \sim 25\ \mathrm{W/(m^2 \cdot {}^\circ C)}$ (the range of natural convection coefficient), and the thermal conductivity of GCr15 is about $k = 15\ \mathrm{W/(m \cdot {}^\circ C)}$. Thus, for typical fatigue specimens we have $\mathrm{Bi} < 0.015 \ll 0.1$. When $\mathrm{Bi} < 0.1$, the temperature in the thickness direction could be considered as uniform without any gradient. In this work, the temperature rise of material during fatigue loading is less than 30 °C, thus the relative material thermodynamic parameters such as mass density ($\rho$), thermal conductivity ($k$) and heat capacity ($C$) will be taken as material constants.

Based on the principle of continuum thermodynamics, the cyclic loading in HCF and VHCF regimes could be taken as an irreversible quasi-static thermo-dynamic process. Thus, the local state equation in HCF and VHCF loading process is [46–48]:

$$\rho C\dot{T} - \nabla \cdot (k\nabla T) = \left(\Sigma - \rho\frac{\partial \psi}{\partial E}\right) : \dot{E} - \rho\frac{\partial \psi}{\partial \zeta} \cdot \dot{\zeta} + \rho T \frac{\partial^2 \psi}{\partial T \partial E} : \dot{E} + \rho T \frac{\partial^2 \psi}{\partial T \partial \zeta} : \dot{\zeta} + q_e \tag{2}$$

where $\psi$ is the specific Helmholtz free energy, $q_e$ denotes the external heat supply (the energy exchange between the material and the environments, which is mainly energy loss through thermal convection and radiation), $\Sigma$ and $E$ are the macroscopic stress and strain. On the left-hand side of Eq. (2), the first term $\rho C\dot{T}$ characterizes the energy storage/loss rate due to temperature variation, and the second term $\nabla \cdot (k\nabla T)$ characterizes the heat loss rate due to heat conduction.

It is assumed that:

$$d_1 = \left(\Sigma - \rho\frac{\partial\psi}{\partial E}\right) : \dot{E} - \rho\frac{\partial\psi}{\partial\zeta}\cdot\dot{\zeta}$$
$$S_{\text{the}} = \rho T\frac{\partial^2\psi}{\partial T\partial E} : \dot{E} \tag{3}$$
$$S_{\text{ic}} = \rho T\frac{\partial^2\psi}{\partial T\partial\zeta} : \dot{\zeta}$$

where, $d_1$ denotes the heat source due to intrinsic dissipation, $S_{\text{the}}$ denotes the heat source due to thermoelastic effect, and $S_{\text{ic}}$ denotes the heat source caused by the interactions between microstructure and temperature variation. $S_{\text{ic}}$ is usually neglected when the temperature rise is relatively low.

Based on the above assumptions, the local state equation of the thin-plate specimen under cyclic loading in HCF and VHCF regimes can be rewritten as:

$$\rho C\dot{T} - k\nabla^2 T = S_{\text{the}} + d_1 + q_e \tag{4}$$

The temperature variation caused by thermoelastic effect is expressed as [30,31]:

$$\Delta T_{\text{e}} = -\frac{\alpha}{\rho C}\cdot T\cdot\Delta\Sigma \tag{5}$$

where $\alpha$ is the thermal expansion coefficient. For the specimens in the present investigation, the temperature variation is lower than 0.1 °C, and the stress ratio $R = -1$. Thus, the heat source $S_{\text{the}}$ is usually neglected for stress-controlled cyclic loadings because the energy generation in a complete load cycle is zero due to thermo-elasticity.

The term $q_{\text{e}}$ characterizes the heat loss of specimens into the surrounding due to temperature rise. The heat loss may be divided into two parts. The first part is the heat conducted into the grip connected with the specimen, and the other part is the heat loss convected into the surrounding through the outer surfaces of the specimen. Assessing the heat loss precisely is very difficult because it is dependent on the boundary conditions and the surrounding. In most cases, a simple linear equation is utilized to characterize the relation between the energy loss and temperature variation:

$$q_{\text{e}} = -\rho C\frac{\theta}{\tau} \tag{6}$$

where $\tau$ is a characteristic time constant related to the heat diffusion from the surface of specimens, and$\theta = T - T_0$, with $T_0$ being the initial temperature.

According to the above assumptions on $S_{\text{the}}$ and $q_e$, Eq. (4) can be rewritten as:

$$\rho C\left(\frac{\partial\theta}{\partial t} + \frac{\theta}{\tau}\right) - k\nabla^2\theta = d_1 \tag{7}$$

In the stable temperature stage, the temperature does not change and $\frac{\partial\theta}{\partial t} = 0$. For uniaxial loading, Eq. (7) is simplified as:

$$\rho C\frac{\theta}{\tau} - k\frac{\partial^2\theta}{\partial x^2} = d_1 \tag{8}$$

The general solution of Eq. (8) is presented in Eq. (9):

$$\theta(x) = A1\cdot e^{rx} + A2\cdot e^{-rx} + A3 \tag{9}$$

where $r = \sqrt{\frac{\rho C}{k\tau}}$, $A1$ and $A2$ are undetermined coefficients, and $A3 = \frac{\tau d_1}{\rho C}$. Thus, the rate of intrinsic dissipation density is obtained as:

$$d_1 = \frac{\rho C}{\tau}A3 = kr^2 A3 \tag{10}$$

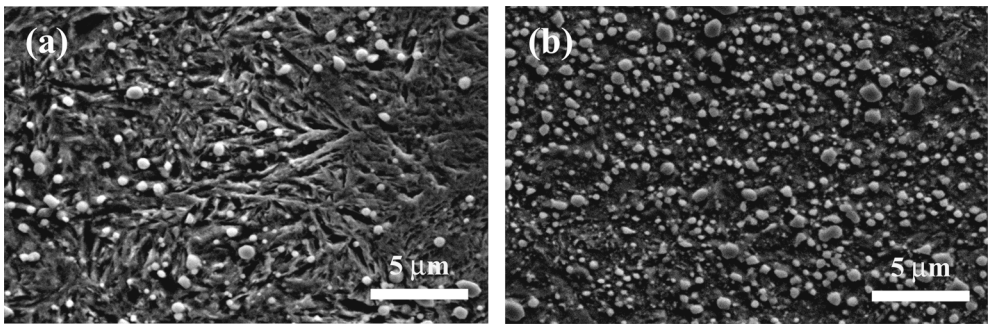


**Fig. 1.** SEM micrographs for two groups of specimens tempered at high and low temperatures. (a) T.T. 150 °C, and (b) T.T. 600 °C.

where parameters $r$ and $A3$ can be obtained by curve fitting of $\theta(x)$ according to Eq. (9). With these parameters, the intrinsic energy dissipation can be deduced.

## 3. Experimental investigation

### 3.1. Material and specimens

The material invested in this work is a high carbon chromium bearing steel (GCr15, similar to SUJ2 of Japanese code or SAE52100 of US code) with the chemical composition (mass percentage) of 1.01C, 1.45 Cr, 0.35 Mn, 0.28Si, 0.015P, 0.01 S and balance Fe. The specimens were heated at 845 °C in vacuum for 120 min, then oil-quenched and tempered in vacuum at 150 °C and 600 °C for 150 min with furnace-cooling, respectively. T.T. stands for tempering temperature in the following text.

The microstructures of the two groups of specimens are shown in Fig. 1. Spheroidal carbides precipitated during tempering for both groups, while the size and number increased evidently at higher tempering temperature. The grain size of prior austenite is about 13.9 μm, obtained from a statistic of 821 grains in the intergranular fracture surfaces of specimens T.T. 150 °C (Details in the supplementary material). It is seen from Fig. 1 that acicular tempered martensite prevails for the specimens T.T. 150 °C, and the average lamellar width is measured as 378 nm. For specimens T.T. 600 °C, recovery occurs in the matrix and the microstructure is tempered sorbite, with a large amount of cementite particles.

Table 1 lists the values of thermodynamical parameters for the two groups of specimens, which are obtained from the experiments. It is shown that the difference in thermodynamics parameters between the two group specimens is negligible.

### 3.2. Experimental method

Cylindrical specimens with a diameter of 6 mm in gauge section were used for the evaluation of mechanical properties of the tested material. The experiment was performed on an MTS 810 testing machine and the applied strain rate is $10^{-4}s^{-1}$. The Vickers hardness of specimens was also measured, during which the applied load is 50 gf and the holding time is 15 s. Table 2 lists the mechanical properties of the two groups of specimens, where $\Sigma_y$ stands for yield strength and $\Sigma_u$ stands for tensile strength.

The geometries of the specimens for fatigue testing are shown in Fig. 2, where the types of thin-plate and round bar were designed, respectively. The surface of specimen was polished by grade 600, 1000, 1500 and 2000 abrasive papers, respectively. Thin-plate specimens were adopted in rapid infrared thermography fatigue experiments, which were conducted on a LETRY PLG − 100 testing machine at room temperature. Sinusoidal waveform mode with a frequency of 120 Hz and the stress ratio of $R = -1$ was used for fatigue loading. The temperature field map on the surfaces of specimen was recorded by an infrared camera Fluke Ti480 and the sampling frequency was set to be 300 Hz. The spectrum response of the facility covers a range from 7.5 μm to 14 μm, with a spatial resolution of 320 × 240 pixels and a sensitivity of 0.05 °C at 30 °C. During the rapid infrared thermography fatigue experiments, loading blocks with increasing magnitude were imposed on a new specimen successively. When the temperature rise was stabilized, a higher loading block was applied (The number of cycles when the temperature was stabilized varies for different loading stress amplitudes.). To ensure a high emissivity, thin black matt coating was painted uniformly on the specimen surface. For the confirmation of the validity of infrared thermography, conventional frequency fatigue test was also carried out, which was performed on a rotating bending machine at room temperature, with a loading frequency of $f = 52.5$ Hz and the stress ratio of $R = -1$.

### 3.3. Experimental results

Fig. 3(a) presents the $S$-$N$ data for the two groups of specimens by conventional fatigue test. The $S$-$N$ curve of the specimens with higher strength (T.T. 150 °C) descends continuously. The point with an arrow means a run-out specimen. The fracture initiates from surface at high stress amplitudes and subsurface defects at low stress amplitudes. The typical patterns of fracture surfaces are presented in the supplementary materials. The fatigue limit or fatigue strength at $N = 10^7$ is about 950 MPa, but below which the specimens continue to break as the loading cycles increase. For the specimens with lower strength (T.T. 600 °C), the $S$-$N$ curve approaches to a horizontal asymptote and clearly has a fatigue limit of 595 MPa.

During fatigue loading, the temperature increased with loading cycles firstly and then stabilized for most of the fatigue lives. The stabilized temperature increment is recorded for different applied stress amplitudes and the results are shown in Fig. 3(b) (The temperature variation curves were provided in the supplementary materials). The tendency of the curve is the same: at relatively lower stress amplitude, the slope is almost the same, and then the slope accelerated significantly at a specific stress amplitude. The abrupt change of temperature evolution could be attributed to the essential change of damage mechanism, which is closely related with the fatigue limit [3–25]. Thus, two linear data fitting lines were used to illustrate the two damage mechanisms, and the interception of the two lines is taken as the fatigue limit. The value of fatigue limit is also presented in the diagrams. The values of fatigue limit obtained

**Table 1**
Values of thermodynamical parameters for two groups of specimens.

| Tempering Temp. (°C) | $\rho$ (kg/m$^3$) | $C_p$(J/(kg•°C)) | $k$ (W/(m•°C)) | $\alpha(10^{-6}$/°C) |
|---|---|---|---|---|
| 150 | 7820 | 546 | 38.2 | 13.3 |
| 600 | 7827 | 553 | 38.6 | 13.1 |

**Table 2**
Mechanical properties of specimens.

| Tempering Temp. (°C) | Micro-Hardness Hv (kgf/mm$^2$) | Young's Modulus (GPa) | Strength (MPa) | |
|---|---|---|---|---|
| | | | $\Sigma_y$ | $\Sigma_u$ |
| 150 | 820 | 208 | NA* | 2372 |
| 600 | 327 | 203 | 909 | 1044 |

* For T.T. 150 °C, the specimens fractured at a strain of 0.14%. Thus, the yield strength is not available.

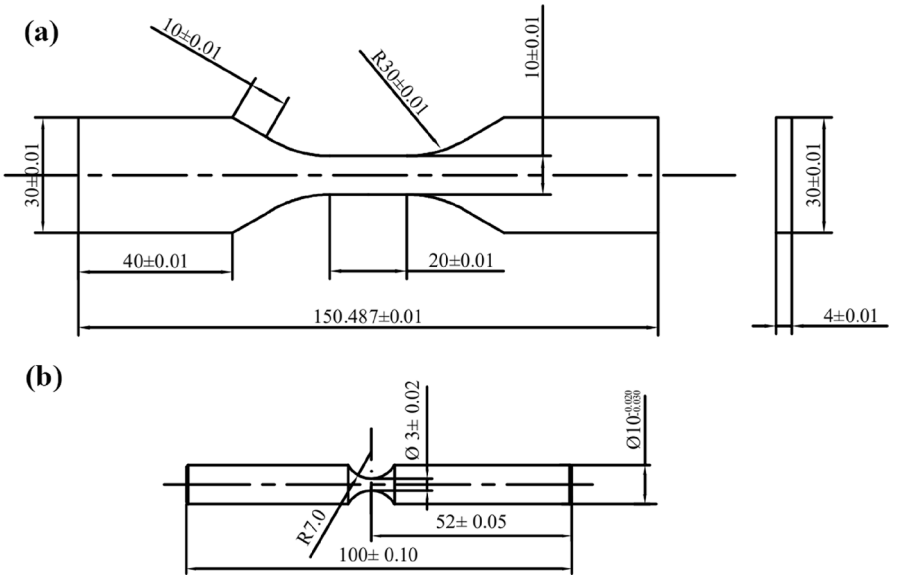


**Fig. 2.** Schematic of specimens used for experiments (dimensions in mm) (a) thermography fatigue experiment, and (b) conventional fatigue test.

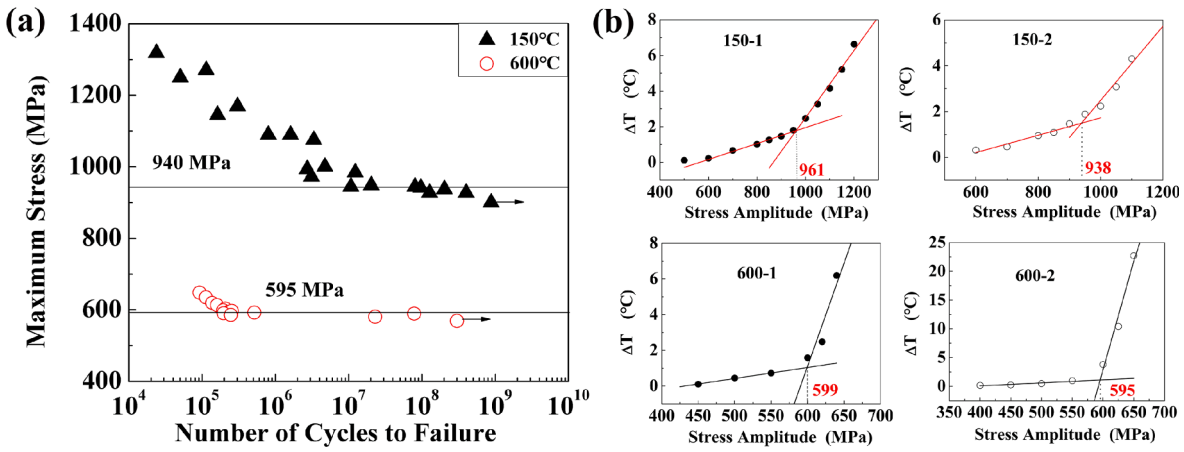


**Fig. 3.** Fatigue limit obtained from different testing methods, (a) data from conventional fatigue test, and (b) temperature rise versus stress amplitude for two groups of specimens.

from two specimens tempered at 150 °C are 961 MPa and 938 MPa, which are close to that obtained by conventional fatigue test (950 MPa). The values of fatigue limit obtained from two specimens tempered at 600 °C are 599 MPa and 595 MPa, which are very close to that obtained by conventional fatigue test (595 MPa).

Although the fatigue properties of many alloys have been well predicted [13–26], the method based on temperature variation often results in a larg scatter band since the temperature field evolution of a specimen at a specific stress amplitude is affected by several factors such as the heat conduction inside the specimen and the heat loss into the environment.

Here, a more fundamental indicator of intrinsic dissipation is derived through the temperature evolution during fatigue loading. The temperature variation at stabilized stage in the gauge part along the specimen length direction in fatigue loading is obtained and

shown in Fig. 4. Eq. (9) is adopted to fit the temperature distribution curve $\theta(x)$, from which parameters $r$ and $A3$ are obtained by curve fitting. With these parameters, the intrinsic energy dissipation can be deduced.

Since the parameters $r$ and $A3$ are obtained, the fatigue intrinsic dissipation is derived via Eq. (10) and the results are shown in Fig. 5. The same methodology is adopted to obtain the fatigue limit, which is 953 MPa and 943 MPa for T.T. 150 °C specimens, and 595.5 MPa and 594.5 MPa for T.T. 600 °C specimens. By comparison with Fig. 3 (b), it is seen that the results obtained by intrinsic dissipation are very close to those by temperature variation.

The comparison with the conventional fatigue test shows the validity of the two rapid infrared thermographies, while the prediction method based on intrinsic dissipation presents higher accuracy. The accuracy of this method is also affected by the properties of materials. For the materials with low strength (T.T. 600 °C, 1044 MPa) and high intrinsic dissipation, the turning point of the intrinsic dissipation is very clear, thus the determination of fatigue limit is distinguishable, and the accuracy of the rapid method is also very high. But for the materials with high strength (T.T. 150 °C, 2372 MPa) and low intrinsic dissipation, the turning point of the intrinsic dissipation is ambiguous. Thus, the determination of fatigue limit could be interfered by the identification of turning point.

## 4. Discussion

### 4.1. Verification of fatigue self-heating by FEM

In the deduction of heat conduction equations of fatigue self-heating, several assumptions were usually used. Thus, it is difficult to verify these assumptions due to the limitation of experimental facilities. However, finite element method (FEM) is a possible approach to study the temperature distribution of a specimen and its evolution with time. Therefore, FEM is utilized to verify the validity of the adopted assumptions and the accuracy of derived parameters from experiments [42].

The FE simulation was performed by a software, COMSOL Multiphysics. The FEM model and relevant thermal boundary conditions are shown in Fig. 6(a), where hexahedron meshing elements were adopted. The boundary conditions and external loads are as follows:

(1) The sections of both end parts for the specimen (A-B and G-H in Fig. 6 (a)) were set to be constant because they were gripped by the clamped parts.

(2) A heat source was applied to the middle gauge part of the specimen (D-E in Fig. 6 (a)) acting as the intrinsic energy dissipation generation.

(3) Heat convection and radiation were adopted within all surfaces of the specimen exposed in air during the experiment.

The key issue in simulating temperature elevation phenomenon during fatigue loading is transforming the applied load into external heat flux density, where the correlation between applied stress amplitude and intrinsic dissipation has already been shown in Fig. 5. The typical temperature distribution of specimen obtained from FEM analysis is presented in Fig. 6 (b). The simulation results show that the maximum temperature appears at the center of gauge part, which coincides well with the experimental results. The temperature along the thickness direction is almost the same, i.e. the temperature distribution of the cross-section along the thickness direction is uniform. The temperature gradient mainly exhibits in the length direction especially in the middle gauge part. The FEM simulation results provide an essential verification for the assumptions adopted in the deduction of heat diffusion equation, where a small Biot number suggests a uniform temperature distribution along the thickness direction.

By using the data obtained from the experiment as input heat flux for simulation, the parameters and temperature distribution data derived from experiments could be verified by FEM simulation results. Thus, the correctness of the theoretical analytical model is validated. The evolution of the temperature rise as a function of applied stress amplitude is presented in Fig. 7 (a). The FEM simulation results suggest that the temperature stabilization state is achieved after a time between 200 and 400 s during fatigue loading, which agree well with the experimental results. Fig. 7 (b) shows the distribution of stabilized temperature variation on the gauge part. It is seen that the temperature distribution characteristics obtained by FEM simulation agree well with experimental data.

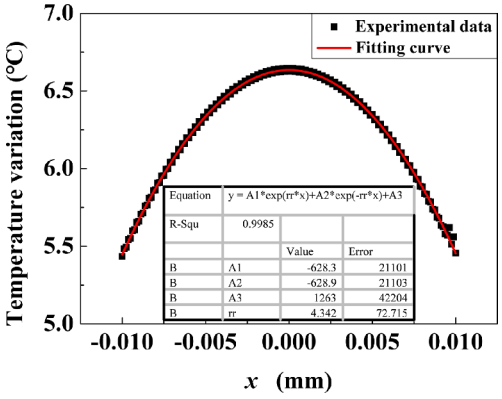


**Fig. 4.** Experimental temperature distribution of specimen along length direction with fitting curve.

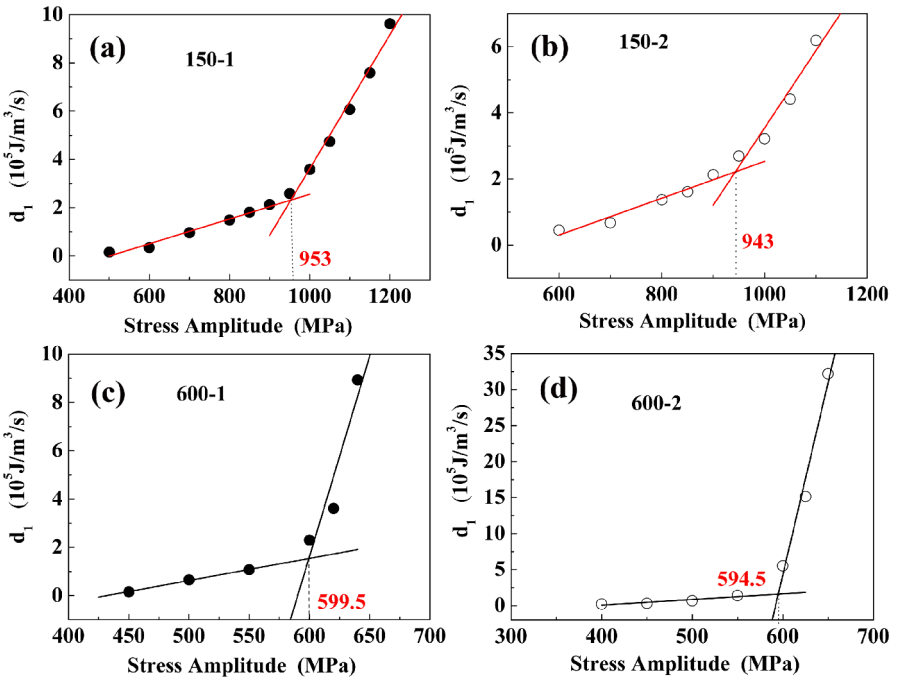


**Fig. 5.** Values of intrinsic dissipation versus stress amplitude for two groups of specimens.

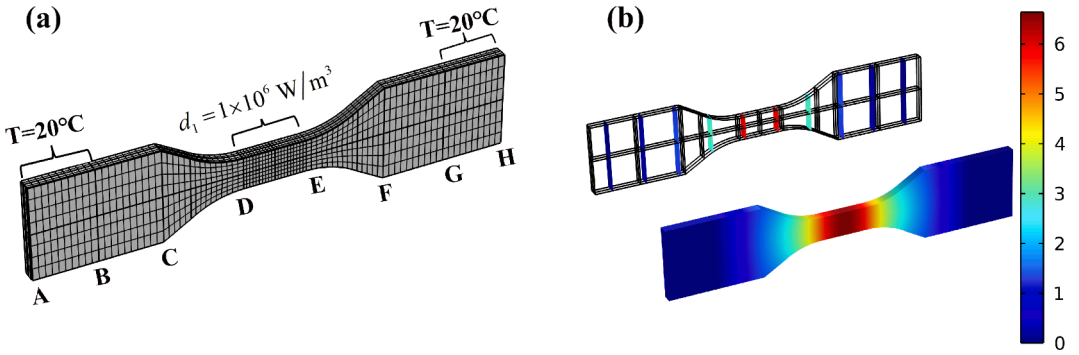


**Fig. 6.** (a) Schematic of FE Model, and (b) FE simulation results of temperature distribution. Upper: cross-section chart, lower: 3D chart.

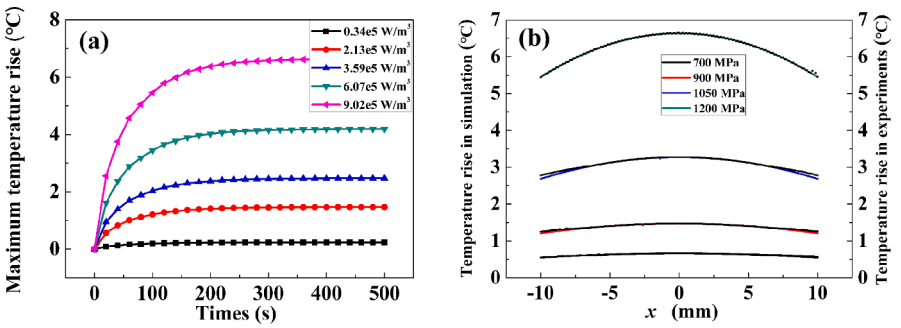


**Fig. 7.** (a) Evolution tendency of specimen surface maximum temperature by simulation, and (b) comparison of stabilized temperature rise distribution between simulations and experiments ($x = 0$ being the middle of gauge part).

### 4.2. Damage mechanism interpreted by dislocation gliding

In this section, the interaction theory between dislocations and point defects is utilized to interpret the self-heating phenomenon during fatigue loading and the corresponding damage mechanisms.

The dislocation lines are initially pinned by point defects as illustrated in Fig. 8(a). The pins inside the dislocation line are generally taken as weak pinning points, while at the two ends of dislocation line the pins are strong pinning points. To move the dislocation lines, the Peierls-Nabarro stress ($\tau_{P-N}$) is needed:

$$\tau_{P-N} = \frac{2G}{1-\nu}\exp\left(-\frac{2\pi w}{b}\right) \tag{11}$$

Eq. (11) presents the minimal stress to vibrate the dislocation lines at 0 K, where $G$ is shear modulus, $\nu$ is Poisson ratio, $w$ is the width of dislocation and $b$ is the magnitude of Burgers vector. $\tau_{P-N}$ is about $10^{-6}$ $G$, which is even lower at higher temperature due to thermal activation. When the local shear stress induced by the external load is larger than $\tau_{P-N}$, the dislocation segments can vibrate between the weak pinning points without breaking off, as shown in Fig. 8 (b). The movements of dislocation lines during fatigue loading are analogous to the vibrating of strings (Granato–Lücke dislocation vibration theory). This motion can be considered as nearly reversible because they do not interact with other vicinal pinning points. Till now the material exhibits pure elastic behavior without intrinsic dissipation macroscopically [26].

Assume $F_m$ is the maximum pinning force between the dislocation lines and weak pinning points, then the unpinning stress $\Gamma$ for the weak pinning shall be [26]:

$$\Gamma = \frac{F_m}{bL}\cdot\frac{\pi^2}{4} = \frac{K\eta Gb}{L_c} \tag{12}$$

where $K$ is a material constant, $\eta$ is the radius mismatch parameter between the solute and solvent atoms, and $L_c$ is the average distance between the weak pinning points. $\Gamma$ is about $10^{-5}$ $G$ at 0 K. When $\sigma_e > \Gamma$ ($\sigma_e$ is the stress applied on the dislocations), the dislocation lines will break away from the constraints of weak pinning points as shown in Fig. 8 (c). The breakaway process continues until all the dislocation segments get rid of the constraints of weak pinning points. Then the whole dislocation line will oscillate between the two strong pinning points, sweeping across an area full of point defects accompanied by continuous pinning-unpinning process, which results in intrinsic energy dissipation. Because the point defects distributed randomly on the dislocation sweep plane, the value of the intrinsic dissipation increases as the area swept by the whole dislocation line increases. Thus, the intrinsic dissipation increases with external load at the macroscopic scale.

In the beginning, the dislocation gliding between two strong pinning points is recoverable because the dislocation lines could be brought back to their equilibrium position under the action of line tension and reverse loading. Thus, no microstructure degradation

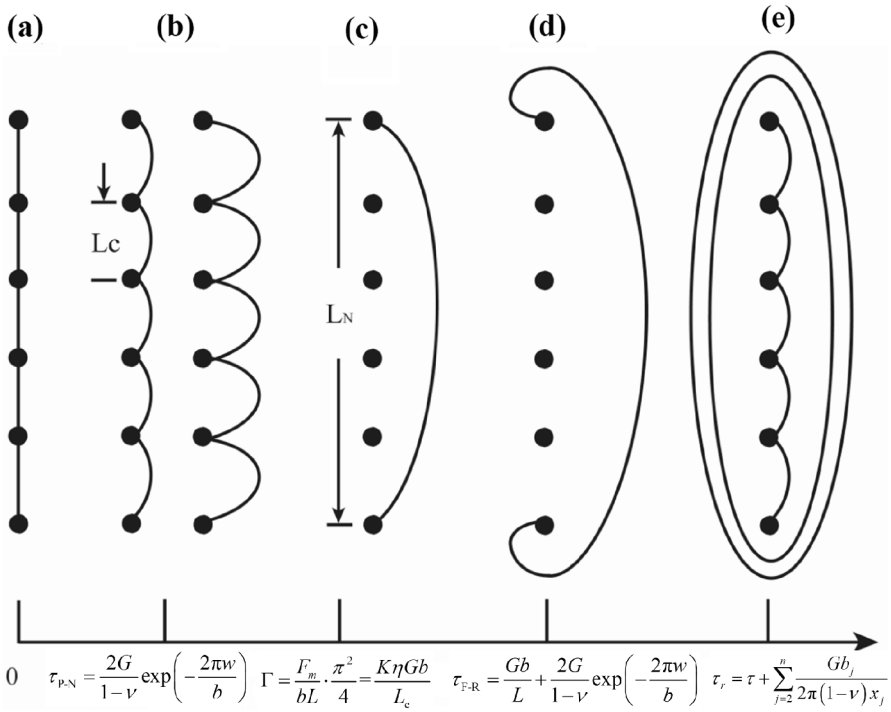


**Fig. 8.** Dislocation vibration and multiplication [49,50].

occurs in this stage and the material exhibits anelasticity macroscopically without damage. When the external load is getting larger, the dislocation lines will sweep over the strong pins and new dislocations will be generated due to the activation of F-R dislocation sources, as shown in Fig. 8(d) and (e). The activation force of an F-R dislocation source is [51,52]:

$$\tau_{\mathrm{F-R}} = \frac{Gb}{L} + \frac{2G}{1-\nu}\exp\left(-\frac{2\pi w}{b}\right) \tag{13}$$

where $L$ is the distance between two strong pins and is about $10^3 b$, which yields $\tau_{\mathrm{F-R}} \approx 10^{-3}G$. It is seen that $\tau_{\mathrm{F-R}}$ is still much lower than the fatigue limit.

Again, when the local shear stress induced by applied stress amplitude is larger than $\tau_{\mathrm{F-R}}$, large amounts of dislocation loops will generate from the source and pile up on grain boundaries, as shown in Fig. 9. Note that $\tau_{\mathrm{F-R}}$ is not a constant. As the number of the dislocation loops $n$ increases, they will have a reaction force $\tau_e$ on the F–R dislocation sources, which makes them harder to be activated after a large number of dislocation loops have been activated. For the leading dislocation loop ($j = 1$), it is in balance under the interaction force of the other dislocation loops and the reaction force of the boundary $\tau_r$:

$$\tau b_1 + \sum_{j=2}^{n} \frac{Gb_j}{2\pi(1-\nu)x_j} - \tau_r b_1 = 0 \tag{14}$$

which yields:

$$\tau_r = \tau + \sum_{j=2}^{n} \frac{Gb_j}{2\pi(1-\nu)x_j} \tag{15}$$

where $\tau_r$ is the action force of all piling-up dislocations on the boundary.

When the action force is larger than the resistance force of the boundary to the piling-up dislocations, i.e.$\tau_r > \tau_0$, the piling-up dislocations will break through the boundary, and the dislocations will be generated continually, leading to final failure if the number of fatigue loading cycles is large enough. For a critical stress amplitude $\tau_f$, after a certain number of loading cycles, large amounts of dislocations will be generated, and the back stress on the F–R dislocation sources is large enough to make them unable to emit any dislocation loops. On the contrary, if $\tau_r < \tau_0$, the piling-up dislocations cannot break through the boundary. Thus, this critical stress amplitude $\tau_f$ is regarded as fatigue limit. It is considered that when the stress amplitude is larger than the activation stress of F–R dislocation sources $\tau_{\mathrm{F-R}}$ but lower than fatigue limit, unrecoverable dislocation multiplication could still appear to cause permanent damage. This damage is just localized to some grains and would not spread to the whole area, and thus failure would not happen for the material.

For T.T. 150 °C specimens, the microstructure of the material is tempered martensite with martensite lamellae in prior austenite grains. For T.T. 600 °C specimens, recovery occurred in the matrix and no martensite features were presented. The large amounts of martensite lamellar boundaries in T.T. 150 °C case would act as strong barriers for dislocation glide and multiplication, thus leading to much lower heat dissipation and high fatigue strength than T.T. 600 °C case.

### 4.3. Microplasticity activation model

In the previous section, a dislocation model was developed to explain the damage accumulation and temperature evolution during

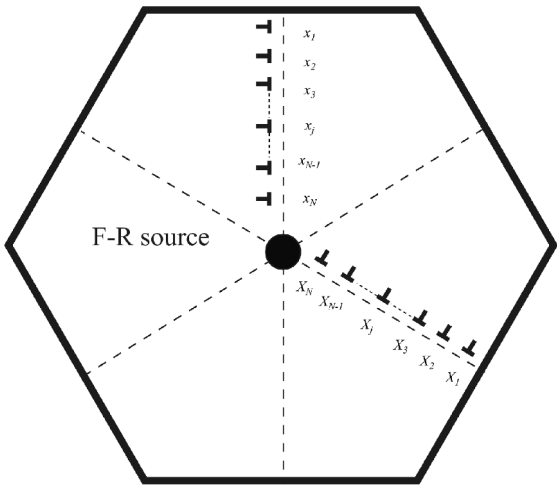


**Fig. 9.** Dynamically piling-up of dislocations emitted from a .
Source [53,54]

fatigue loading. Although a two linear segment theory based on fatigue self-heating was proposed to assess the fatigue limit [30–43], the relation of power function seems more suitable for describing the variation of temperature variation with stress amplitude. For a much more detailed description, a two probabilistic multiscale model is adopted to explain these phenomena.

As described above, the applied stress amplitude is lower than the macroscopic yield stress of materials in HCF and VHCF regimes, and the material is still in elastic deformation macroscopically. However, at some isolated grains localized damage accumulation or microplasticity may emerge, which will result in considerable energy dissipation and temperature rise. Therefore, to establish the related between the damage accumulation and the intrinsic dissipation is very beneficial for assessing the fatigue properties of materials [43].

Lemaitre et al. [55] first proposed a representative volume element (RVE) model to assess the local damage accumulation quantitatively. The schematic diagram of local damage emerging zones is demonstrated in Fig. 10. An RVE is divided into two zones, the elastic matrix and the elasto-plastic inclusion where the microplasticity occurs. The macroscopic stress and strain are defined by $\Sigma$ and $E$, while the microscopic stress and strain are defined by $\sigma$ and $\varepsilon$, respectively. The two zones are assumed to have the same elastic modulus ($E_{\mathrm{M}}$, $\mu$) and Poisson's ratio ($\nu$). But the microscopic yield stress $\sigma_{\mathrm{ym}}$ of the elasto-plastic inclusion is much lower than $\Sigma_{\mathrm{y}}$ of the elastic matrix. This means that when microplasticity takes place in the elasto-plastic inclusion part, the majority of deformation in RVE is still elastic macroscopically. By introducing the concept of localization and homogenization, the relation between the macroscopic stress and plastic strain is derived as follows [43,55]:

$$\sigma = \Sigma - 2\mu(1-\beta)\varepsilon_{\mathrm{P}} \tag{16}$$

where $\beta = \frac{2(4-5\nu)}{15(1-\nu)}$ (given by Eshelby referred to [43]), and $\varepsilon_{\mathrm{p}}$ is the microplastic strain.

The yield stress levels for various RVEs are assumed to be different even in a specimen [56,57]. When the applied stress amplitude is larger than $\sigma_{\mathrm{ym}}$ (the microscopic yield stress of the elastic–plastic zone), the RVE will be activated and produce plastic energy dissipation. It is reasonable that the higher the applied stress amplitude is, the more RVE sites will be activated, which consequently results in larger dissipated energy and higher temperature rise. The local damage accumulation occurs on microscopic scale, while the activated RVE is assumed to conform to a Poisson point process (PPP) distribution [58]. Then the probability of the activated RVEs in a zone $\Omega$ of $V_\Omega$ is [58]:

$$P_k(\Omega) = \frac{[-N(\Omega)]^k}{k!}\exp[-N(\Omega)], \; N(\Omega) = \lambda V_\Omega \tag{17}$$

where $N(\Omega)$ is the activated number of RVEs in zone $\Omega$, and $\lambda$ is the average number of activated RVEs per unit volume. It is assumed that the activated number increases with external load. Thus, $\lambda$ is defined as a power function of stress amplitude:

$$\lambda(\Sigma_0) = \frac{1}{V_0}\left(\frac{\Sigma_0}{S_0}\right)^m = \frac{1}{V_0 S_0^m}\Sigma_0^m \tag{18}$$

where $\Sigma_0$ is the external load, $V_0{S_0}^m$ and $m$ are two material constants larger than 0.

Different materials will correspond to different values of $V_0{S_0}^m$. From Eq. (18), the term $V_0{S_0}^m$ provides a parameter to describe the resistance of microplasticity activation. As a result, the weakest link theory is utilized to derive fatigue limits, where at least one active RVE site is needed. Through Eq. (17), the failure probability subjected to different stress amplitudes is [57,59].

$$P_{\mathrm{F}} = P_{k\geqslant 1}(V) = 1 - \exp[-\lambda V] = 1 - \exp\left(-\frac{V}{V_0}\left(\frac{\Sigma_{\mathrm{a}}}{S_0}\right)^m\right) \tag{19}$$

Thus, the fatigue limit is derived [57,59]:

$$\overline{\Sigma}_\infty = S_0\left(\frac{V_0}{V}\right)^{\frac{1}{m}}\Gamma\left(1+\frac{1}{m}\right) \tag{20}$$

The temperature variation of the specimen will approach to a steady one during fatigue loading process, which is given as [57,59]:

$$\overline{\theta} = \eta V_0 \frac{m}{(m+1)(m+2)}\frac{\Sigma_0^{m+2}}{\left(V_0^{1/m}S_0\right)^m} \tag{21}$$

where $\eta$ is a constant relative to the specimen.

The curve of temperature variation versus stress amplitude could be obtained by infrared thermography. Thus, the value of $m$ can be derived through data fitting, as shown in Fig. 11. If we take the abrupt turning point of the temperature variation as fatigue limit $\overline{\Sigma}_\infty$, where the variation is less than 10% compared with the results obtained by conventional fatigue experiments, and the effective specimen volume $V_0$ is already determined. Then the parameter $V_0S_0^m$ is derived. The results are listed in Table 3. It is seen that the values of $S_0V_0^{1/m}$ are in good consistence for the same material group, which are 1448 and 1401 for T.T. 150 °C specimens, and 660.8 and 661.5 for T.T. 600 °C specimens. The results also indicate that T.T. 150 °C specimens show greater resistance to microplasticity activation than T.T. 600 °C specimens.

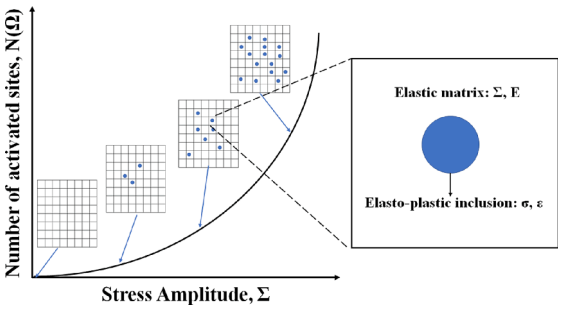


**Fig. 10.** Schematic of localized damage accumulation with stress amplitude [43].

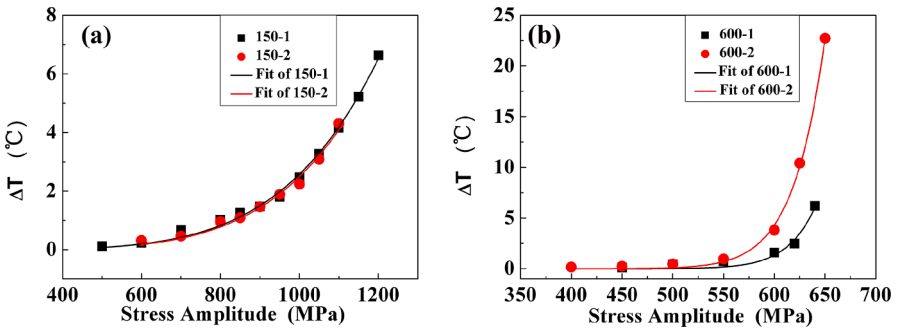


**Fig. 11.** Experimental data and fitting curves of temperature variation.

**Table 3**
Calculation results by microplasticity activation model.

| Specimen | $m$ | $\overline{\Sigma}_{\infty}$(MPa) | $S_0V_0^{1/m}$ |
|---|---|---|---|
| 150–1 | 5.102 (4.766, 5.437)* | 961 | 1448 |
| 150–2 | 5.225 (4.472, 5.979) * | 938 | 1401 |
| 600–1 | 22.44 (10.00, 34.87) * | 599 | 660.8 |
| 600–2 | 20.79 (18.88, 22.71) * | 595 | 661.5 |

* The values in brackets present the range of 95% confidence interval.

## 5. Conclusions

In this paper, the energy dissipation during HCF and VHCF processes was detected and utilized to assess the fatigue limit of a high carbon chromium bearing steel with two strength levels. The temperature variation of the specimen during fatigue loading is recorded by infrared thermography. The maximum temperature variation and the temperature distribution along the specimen surface were measured to obtain the intrinsic energy dissipation under different stress amplitudes. Main results are summarized as follows:

1. Two methods based on the maximum temperature variation and intrinsic energy dissipation are used to predict the fatigue limit, and both present good coincidence with those obtained by conventional fatigue tests. The method based on the intrinsic energy dissipation presents less scatter and higher accuracy than the method based on the maximum temperature variation, which indicates that the fatigue intrinsic dissipation is a more reasonable damage indicator.
2. FEM simulation is utilized to assess the self-heating process during fatigue loading, which coincides well with the experimental data and characterizes the effect of stress amplitude on temperature variation effectively.
3. A dislocation multiplication model is developed to explain the damage accumulation evolution during fatigue loading, which demonstrates that the activation of F-R dislocation sources may intrigue localized microplasticity and damage, but it is not sufficient to cause fatigue failure. The resistance of grain boundary against dislocation piling-up is crucial in determining fatigue strength. The tempered martensite for the material group tempered at 150 °C acts as great barriers for dislocation gliding and multiplication, which makes the group possess much larger fatigue strength than that for the material group tempered at 600 °C.
4. A two probabilistic multiscale model is adopted to assess the fatigue limit and the microplasticity activation resistance of a material. A parameter $S_0V_0^{1/m}$ is proposed to characterize the resistance of microplasticity activation, which presents good consistence for the material. The results also indicate that the T.T. 150 °C specimens show greater resistance of microplasticity activation than that of T.T. 600 °C specimens.

## CRediT authorship contribution statement

**Aiguo Zhao:** Resources, Writing – original draft, Investigation, Conceptualization. **Jijia Xie:** Investigation, Conceptualization. **Yingxin Zhao:** Methodology, Validation. **Chuang Liu:** Visualization, Formal analysis. **Junchen Zhu:** Software, Project administration, Resources. **Guian Qian:** Validation, Conceptualization. **Shuguang Wang:** Funding acquisition, Supervision, Writing – review & editing. **Youshi Hong:** Writing – review & editing, Resources, Funding acquisition, Conceptualization.

## Declaration of Competing Interest

The authors declare that they have no known competing financial interests or personal relationships that could have appeared to influence the work reported in this paper.

## Acknowledgements

This paper was supported by the National Natural Science Foundation of China (Nos. 11932020 and 51678302).

## Appendix A. Supplementary data

Supplementary data to this article can be found online at https://doi.org/10.1016/j.engfracmech.2022.108460.

## References

[1] Suresh S, editor. Fatigue of materials. Cambridge: Cambridge University Press; 1998.
[2] Pan X, Hong Y. High-cycle and very-high-cycle fatigue behaviour of a titanium alloy with equiaxed microstructure under different mean stresses. Fatigue Fract Eng Mater Struct 2019;42(9):1950–64.
[3] Luong MP. Fatigue limit evaluation of metal using an infrared thermographic technique. Mech Mater 1998;28(1–4):155–63.
[4] La Rosa G, Risitano A. Thermographic methodology for rapid determination of the fatigue limit of materials and mechanical components. Int J Fatigue 2000;22(1):65–73.
[5] Yang W, Guo Q, Fan J, Guo X, Zhao Y. Effect of aging temperature on energy dissipation and high-cycle fatigue properties of FV520B stainless steel. Eng Fract Mech 2021;242:107464. https://doi.org/10.1016/j.engfracmech.2020.107464.
[6] Amiri M, Khonsari MM. Rapid determination of fatigue failure based on temperature evolution: Fully reversed bending load. Int J Fatigue 2010;32(2):382–9.
[7] Teng Z, Wu H, Boller C, Starke P. Thermodynamic entropy as a marker of high-cycle fatigue damage accumulation: Example for normalized SAE 1045 steel. Fatigue Fract Eng Mater Struct 2020;43(12):2854–66.
[8] Palumbo D, De Finis R, Ancona F, Galietti U. Damage monitoring in fracture mechanics by evaluation of the heat dissipated in the cyclic plastic zone ahead of the crack tip with thermal measurements. Eng Fract Mech 2017;181:65–76.
[9] Chrysochoos A, Louche H. An infrared image processing to analyze the calorific effects accompanying strain localization. Int J Eng Sci 2000;38(16):1759–88.
[10] Louche H, Chrysochoos A. Thermal and dissipative effects accompanying Lüders band propagation. Mater Sci Eng, A 2001;307(1-2):15–22.
[11] Risitano A, Risitano G. Cumulative damage evaluation of steel using infrared thermography. Theor Appl Fract Mec 2010;54(2):82–90.
[12] Boulanger T, Chrysochoos A, Mabru C, Galtier A. Calorimetric analysis of dissipative and thermoelastic effects associated with the fatigue behavior of steels. Int J Fatigue 2004;26(3):221–9.
[13] Meneghetti G. Analysis of the fatigue strength of a stainless steel based on the energy dissipation. Int J Fatigue 2007;29(1):81–94.
[14] Morabito A, Chrysochoos A, Dattoma V, Galietti U. Analysis of heat sources accompanying the fatigue of 2024 T3 aluminum alloys. Int J Fatigue 2007;29(5):977–84.
[15] Maquin F, Pierron F. Heat dissipation measurements in low stress cyclic loading of metallic materials: From internal friction to micro-plasticity. Mech Mater 2009;41(8):928–42.
[16] Charkaluk E, Constantinescu A. Dissipative aspects in high cycle fatigue. Mech Mater 2009;41(5):483–94.
[17] Connesson N, Maquin F, Pierron F. Experimental energy balance during the first cycles of cyclically loaded specimens under the conventional yield stress. Exp Mech 2011;51(1):23–44.
[18] Connesson N, Maquin F, Pierron F. Dissipated energy measurements as a marker of microstructural evolution: 316L and DP600. Acta Mater 2011;59(10):4100–15.
[19] Meneghetti G, Ricotta M. The use of the specific heat loss to analyze the low- and high-cycle fatigue behavior of plain and notched specimens made of a stainless steel. Eng Fract Mech 2012;81:2–16.
[20] Meneghetti G, Ricotta M, Atzori B. A synthesis of the push-pull fatigue behavior of plain and notched stainless steel specimens by using the specific heat loss. Fatigue Fract Eng Mater Struct 2013;36(12):1306–22.
[21] Pierron Q, Maitournam H, Raoult I. Thermographic approach for high cycle fatigue of seam welded steel joints under variable amplitude loadings. Fatigue Fract Eng Mater Struct 2020;43:2966–83.
[22] Huang ZY, Wang QY, Wagner D, Bathias C. A very high cycle fatigue thermal dissipation investigation for titanium alloy TC4. Mater Sci Eng A 2014;600:153–8.
[23] Yan ZF, Zhang HX, Wang WX, He XL, Liu XQ, Wu GH. Temperature evolution mechanism of AZ31B magnesium alloy during high-cycle fatigue process. Theor Appl Fract Mech 2014;70:30–8.
[24] Blanche A, Chrysochoos A, Ranc N, Favier V. Dissipation assessments during dynamic very high cycle fatigue tests. Exp Mech 2015;55(4):699–709.
[25] Xu Z, Zhang H, Yan Z, Liu F, Liaw PK, Wang W. Three-point-bending fatigue behavior of AZ31B magnesium alloy based on infrared thermography technology. Int J Fatigue 2017;95:156–67.
[26] Gremaud G. Dislocation - point defect interactions. Mater Sci Forum 2001;366:178–246.
[27] Fan GD, Zheng MY, Hu XS, Wu K, Gan WM, Brokmeier HG. Internal friction and microplastic deformation behavior of pure magnesium processed by equal channel angular pressing. Mater Sci Eng A 2013;561:100–8.
[28] Vinogradov A, Yasnikov IS. On the nature of acoustic emission and internal friction during cyclic deformation of metals. Acta Mater 2014;70:8–18.
[29] Meneghetti G, Ricotta M. Estimating the intrinsic dissipation using the second harmonic of the temperature signal in tension-compression fatigue: Part I. Theory Fatigue Fract Eng Mater Struct 2021;44:2168–85.
[30] Guo Q, Guo X, Fan J, Syed R, Wu C. An energy method for rapid evaluation of high-cycle fatigue parameters based on intrinsic dissipation. Int J Fatigue 2015;80:136–44.

[31] Guo Q, Guo X. Research on high-cycle fatigue behavior of FV520B stainless steel based on intrinsic dissipation. Mater Design 2016;90:248–55.
[32] Torabian N, Favier V, Ziaei-Rad S, Dirrenberger J, Adamski F, Ranc N. Thermal response of DP600 dual-phase steel under ultrasonic fatigue loading. Mater Sci Eng A 2016;677:97–105.
[33] Wang XG, Crupi V, Jiang C, Feng ES, Guglielmino E, Wang CS. Energy-based approach for fatigue life prediction of pure copper. Int J Fatigue 2017;104:243–50.
[34] Wang XG, Feng ES, Jiang C. A microplasticity evaluation method in very high cycle fatigue. Int J Fatigue 2017;94:6–15.
[35] Fan J, Guo X, Zhao Y. An energetic method to evaluate the macro and micro high-cycle fatigue behavior of the aluminum alloy. J Mech Eng Sci 2018;232(8):1456–69.
[36] Wang XG, Ran HR, Jiang C, Fang QH. An energy dissipation-based fatigue crack growth model. Int J Fatigue 2018;114:167–76.
[37] Fan J, Zhao Y, Guo X. A unifying energy approach for high cycle fatigue behavior evaluation. Mech Mater 2018;120:15–25.
[38] Yang W, Guo X, Guo Q, Fan J. Rapid evaluation for high-cycle fatigue reliability of metallic materials through quantitative thermography methodology. Int J Fatigue 2019;124:461–72.
[39] Salimi H, Pourgol-Mohammad M, Yazdani M. Metal fatigue assessment based on temperature evolution and thermodynamic entropy generation. Int J Fatigue 2019;127:403–16.
[40] Mehdizadeh M, Khonsari MM. On the role of internal friction in low-and high-cycle fatigue. Int J Fatigue 2018;114:159–66.
[41] Teng Z, Wu H, Boller C, Starke P. Thermography in high cycle fatigue short-term evaluation procedures applied to a medium carbon steel. Fatigue Fract Eng Mater Struct 2020;43(3):515–26.
[42] Guo Q, Zaïri F, Yang W. Evaluation of intrinsic dissipation based on self-heating effect in high-cycle metal fatigue. Int J Fatigue 2020;139:105653. https://doi.org/10.1016/j.ijfatigue.2020.105653.
[43] Teng Z, Wu H, Boller C, Starke P. A unified fatigue life calculation based on intrinsic thermal dissipation and microplasticity evolution. Int J Fatigue 2020;131:105370. https://doi.org/10.1016/j.ijfatigue.2019.105370.
[44] ASHRAE, Inc. 2009 ASHRAE handbook: fundamentals.: American Society of Heating, Refrigeration and Air-Conditioning Engineers, 2009.
[45] Holman. Heat transfer. McGraw-Hill 2010.
[46] Coleman BD, Noll W. The thermodynamics of elastic materials with heat conduction and viscosity. Arch Ration Mech Anal 1963;13(1):167–78.
[47] Rice JR. Inelastic constitutive relations for solids: an internal-variable theory and its application to metal plasticity. J Mech Phys Solids 1971;19(6):433–55.
[48] Horstemeyer MF, Bammann DJ. Historical review of internal state variable theory for inelasticity. Int J Plast 2010;26(9):1310–34.
[49] Granato A, Lücke K. Theory of mechanical damping due to dislocations. J Appl Phys 1956;27(6):583–93.
[50] Granato A, Lücke K. Application of dislocation theory to internal friction phenomena at high frequencies. J Appl Phys 1956;27(7):789–805.
[51] Frank FC, Read WT. Multiplication processes for slow moving dislocations. Phys Rev 1950;79(4):722–3.
[52] Burton WK, Cabrera N, Frank FC. The growth of crystals and the equilibrium structure of their surfaces. Philos Trans R Soc A 1951;243:299–358.
[53] Tanaka K, Mura T. A dislocation model for fatigue crack initiation. J Applied Mechanics 1981;48:097–103.
[54] Mura T, Nakasone Y. A theory of fatigue crack initiation in solids. J Applied Mechanics 1990;57:1–6.
[55] Lemaitre J, Sermage JP, Desmorat R. A two scale damage concept applied to fatigue. Int J Fract 1999;97:67–81.
[56] Doudard C, Calloch S, Cugy P, Galtier A, Hild F. A probabilistic two-scale model for high-cycle fatigue life predictions. Fatigue Fract Eng Mater Struct 2005;28(3):279–88.
[57] Doudard C, Hild F, Calloch S. A probabilistic model for multiaxial high cycle fatigue. Fatigue Fract Eng Mater Struct 2007;30(2):107–14.
[58] Gulino R, Phoenix S. Weibull strength statistics for graphite fibers measured from the break progression in a model graphite/glass/epoxy microcomposite. J Mater Sci 1991;26:3107–18.
[59] Poncelet M, Doudard C, Calloch S, Weber B, Hild F. Probabilistic multiscale models and measurements of self-heating under multiaxial high cycle fatigue. J Mech Phys Solids 2010;58(4):578–93.